

# Single-step quantitative susceptibility mapping with variational penalties

Itthi Chatnuntawech<sup>a\*</sup>, Patrick McDaniel<sup>a</sup>, Stephen F. Cauley<sup>b,c</sup>, Borjan A. Gagoski<sup>c,d</sup>, Christian Langkammer<sup>e</sup>, Adrian Martin<sup>f</sup>, P. Ellen Grant<sup>c,d</sup>, Lawrence L. Wald<sup>b,c,g</sup>, Kavin Setsompop<sup>b,c</sup>, Elfar Adalsteinsson<sup>a,g</sup> and Berkin Bilgic<sup>b,c</sup>



Quantitative susceptibility mapping (QSM) estimates the underlying tissue magnetic susceptibility from the gradient echo (GRE) phase signal through background phase removal and dipole inversion steps. Each of these steps typically requires the solution of an ill-posed inverse problem and thus necessitates additional regularization. Recently developed single-step QSM algorithms directly relate the unprocessed GRE phase to the unknown susceptibility distribution, thereby requiring the solution of a single inverse problem. In this work, we show that such a holistic approach provides susceptibility estimation with artifact mitigation and develop efficient algorithms that involve simple analytical solutions for all of the optimization steps. Our methods employ total variation (TV) and total generalized variation (TGV) to jointly perform the background removal and dipole inversion in a single step. Using multiple spherical mean value (SMV) kernels of varying radii permits high-fidelity background removal whilst retaining the phase information in the cortex. Using numerical simulations, we demonstrate that the proposed single-step methods reduce the reconstruction error by up to 66% relative to the multi-step methods that involve SMV background filtering with the same number of SMV kernels, followed by TV- or TGV-regularized dipole inversion. *In vivo* single-step experiments demonstrate a dramatic reduction in dipole streaking artifacts and improved homogeneity of image contrast. These acquisitions employ the rapid three-dimensional echo planar imaging (3D EPI) and Wave-CAIPI (controlled aliasing in parallel imaging) trajectories for signal-to-noise ratio-efficient whole-brain imaging. Herein, we also demonstrate the multi-echo capability of the Wave-CAIPI sequence for the first time, and introduce an automated, phase-sensitive coil sensitivity estimation scheme based on a 4-s calibration acquisition. Copyright © 2016 John Wiley & Sons, Ltd.

Additional supporting information may be found in the online version of this article at the publisher's web site.

**Keywords:** quantitative susceptibility mapping (QSM); total variation (TV); total generalized variation (TGV); alternating direction method of multipliers (ADMM); Wave-CAIPI

## INTRODUCTION

High-resolution phase images derived from gradient echo (GRE) acquisitions provide a dramatic contrast boost between and

within gray matter and white matter, compared with conventional magnitude imaging (1). However, the phase contrast at a particular location stems from non-local effects with contributions from surrounding voxels (2–4). These non-local effects make it difficult to robustly relate features in the phase images to the underlying anatomical structures (5). Nonetheless, the same GRE data also lend themselves to quantitative

\* Correspondence to: I. Chatnuntawech, Massachusetts Institute of Technology, Room 36-776A, 77 Massachusetts Avenue, Cambridge, MA 02139, USA. E-mail: ichtatnun@mit.edu

a I. Chatnuntawech, P. McDaniel, E. Adalsteinsson  
Department of Electrical Engineering and Computer Science, Massachusetts Institute of Technology, Cambridge, MA, USA

b S. F. Cauley, L. L. Wald, K. Setsompop, B. Bilgic  
A. A. Martinos Center for Biomedical Imaging, Department of Radiology; Massachusetts General Hospital, Charlestown, MA, USA

c S. F. Cauley, B. A. Gagoski, P. E. Grant, L. L. Wald, K. Setsompop, B. Bilgic  
Harvard Medical School, Boston, MA, USA

d B. A. Gagoski, P. E. Grant  
Fetal–Neonatal Neuroimaging & Developmental Science Center, Boston Children's Hospital, Harvard Medical School, Boston, MA, USA

e C. Langkammer  
Department of Neurology, Medical University of Graz, Graz, Austria

f A. Martin  
Applied Mathematics, Universidad Rey Juan Carlos, Mostoles, Madrid, Spain

g L. L. Wald, E. Adalsteinsson  
Harvard-MIT Health Sciences and Technology, Massachusetts Institute of Technology, Cambridge, MA, USA

**Abbreviations used:** 3D, three-dimensional; ADMM, alternating direction method of multipliers; CAIPI, controlled aliasing in parallel imaging; COSMOS, calculation of susceptibility through multiple orientation sampling; CSF, cerebrospinal fluid; EPI, echo planar imaging; FOV, field of view; GRE, gradient echo; MEDI, morphology-enabled dipole inversion; pcg, preconditioned conjugate gradients; PDF, projection onto dipole fields; QSM, quantitative susceptibility mapping; RMSE, root-mean-square error; SHARP, sophisticated harmonic artifact reduction for phase data; SMV, spherical mean value; SNR, signal-to-noise ratio; SVD, singular value decomposition; TV, total variation; TGV, total generalized variation.

susceptibility mapping (QSM), which estimates the underlying tissue magnetic susceptibility that gives rise to this phase contrast. QSM resolves the confounding non-local bias in the phase images and provides a novel quantitative biomarker in the brain. Susceptibility mapping has already shown potential in the study of brain development and aging (6–8), the evaluation and monitoring of neurodegenerative and neuro-inflammatory diseases (9–11) and the estimation of vessel oxygenation (12–14).

However, QSM estimation from the acquired GRE phase signal entails successive applications of multiple post-processing steps. These steps include phase unwrapping, removal of phase contributions from background sources and the solution of an ill-posed inverse problem relating the tissue phase to the magnetic susceptibility distribution (dipole inversion). Efficient phase unwrapping techniques have been developed to resolve the ambiguity caused by the  $2\pi$  periodicity of the acquired GRE phase (15,16). The background component of the unwrapped phase, mostly stemming from the air–tissue and air–bone interfaces, is up to two orders of magnitude larger than the tissue component, and thus needs to be removed for successive processing. Popular background removal techniques include sophisticated harmonic artifact reduction for phase data [SHARP, aka spherical mean value (SMV) filtering] (17) and projection onto dipole fields (PDF) (18). Finally, an inverse problem needs to be solved to estimate the underlying susceptibility distribution from the background-removed unwrapped tissue phase. To mitigate the streaking artifacts caused by the ill-posed inversion, weighted quadratic smoothing (i.e.  $\ell_2$  penalty on the image gradients) (19,20), weighted total variation (TV) (21–25) and total generalized variation (TGV) (26–28) regularized QSMs have been proposed. As these regularized QSMs impose sparsity or smoothness assumptions on the image gradients, streaking artifact mitigation comes at a cost of some amount of image blurring. To prevent both image blurring and streaking artifacts, additional GRE volumes acquired at different head orientations relative to the MRI magnetic field can be used. The combination of these GRE volumes results in an over-determined inverse problem, which can be solved without regularization. This technique is termed calculation of susceptibility through multiple orientation sampling (COSMOS) and yields QSM images with exquisite detail and contrast (5,22,29–31). Despite the marked improvement in image quality relative to single-orientation-regularized QSMs, multi-orientation QSM comes at a cost of a significant increase in data acquisition time (32).

More recently, a new class of QSM algorithm that directly relates the GRE phase signal to the unknown susceptibility distribution has been proposed (27,28,33–35). By performing the background phase removal and dipole inversion in a single step, these algorithms prevent potential error propagation across successive operations. As a single regularizer acts on both operations, a separate thresholding parameter for SMV background filtering is no longer needed. In ref. (33), a single-step QSM reconstruction technique which combined single-kernel SMV filtering with weighted quadratic smoothing was proposed. By extending the morphology-enabled dipole inversion (MEDI) technique (21–23), a differential QSM method was developed to bypass the phase unwrapping and background phase removal steps (34). Using TGV regularization, a single-step QSM model was developed in refs. (27,28) to mitigate the staircasing artifacts often observed in the TV-based reconstructions. This single-step TGV optimization problem was

efficiently solved using a primal–dual algorithm that finds a saddle point of general convex–concave problems (36). In ref. (35), multiple SMV kernels were incorporated into the single-step QSM with quadratic smoothing regularization to reduce the loss of cortical phase information.

In this work, we develop a new single-step QSM model that combines the advantages of multiple SMV kernels and variational penalties that consist of TV and TGV regularizations. The main contributions of this work are as follows.

1. TV- and TGV-regularized single-step QSMs with multiple SMV kernels are proposed. Using both numerical and *in vivo* data, we demonstrate that the proposed single-step QSM methods better mitigate dipole artifacts with improved homogeneity of image contrast than the conventional QSM algorithms that involve multiple sequential post-processing steps.
2. We introduce the multi-echo version of the Wave-CAIPI (controlled aliasing in parallel imaging) sequence (30,37) that allows rapid three-dimensional (3D) GRE imaging with high encoding efficiency. The multi-echo extension of Wave-CAIPI fully utilizes TR to sample multiple echoes, which are then combined to improve the magnitude and phase signal-to-noise ratios (SNRs). Furthermore, we propose a novel coil sensitivity estimation scheme that is fully automated and allows high-quality parallel imaging whilst preserving the image phase. This relies on a rapid, 4-s calibration scan, which is followed by phase-sensitive channel compression (38) and ESPIRiT coil sensitivity estimation (39).
3. Fast solvers for the proposed single-step model are developed based on alternating direction method of multipliers (ADMM) and variable splitting (40–48). Special structures of the matrices in the models are exploited so that all the subproblems can be solved using closed-form solutions.
4. Accompanying data and MATLAB implementation are made available at: [martinos.org/~berkin/TGV\\_SS\\_QSM.zip](http://martinos.org/~berkin/TGV_SS_QSM.zip)

## THEORY

### TV- and TGV-regularized single-step QSM with multiple SMV kernels

The underlying magnetic susceptibility distribution is conventionally estimated from the GRE phase using multiple sequential post-processing steps. First, the acquired raw phase  $\phi$  is unwrapped (15,16). Then, the background phase is removed to obtain the unwrapped tissue phase  $\phi_{u, \text{tissue}}$  (17,18). Finally, the following system of linear equations is solved to estimate the underlying susceptibility distribution  $\chi$  from  $\phi_{u, \text{tissue}}$ :

$$d * \chi = \phi_{u, \text{tissue}} \quad [1]$$

where  $d$  is the spatial dipole kernel and  $*$  denotes the 3D convolution.

Recently, QSM algorithms that estimate the underlying  $\chi$  in a single step have been proposed to prevent potential error propagation between the subsequent steps. In this work, we propose to estimate the underlying  $\chi$  in a single step by solving the following optimization problem:

$$\min_{\chi} \frac{1}{2} \sum_i \|M_i(h_i * d * \chi) - M_i(h_i * \Psi(\phi))\|_2^2 + R(\chi) \quad [2]$$

$\Psi$  is the Laplacian unwrapping operator defined as  $\Psi(\phi) = \Delta^{-1} \cdot \text{Im}(e^{-j\phi} \cdot \Delta e^{j\phi})$ , where  $\Delta$  is the discrete Laplacian.  $h_i$  is

an SMV kernel for the  $i$ th reliable phase region, defined as  $h_i = \delta - \rho_i$  where  $\delta$  is a unit impulse and  $\rho_i$  is a non-negative radially symmetric, normalized kernel (17).  $M_i$  is a diagonal matrix that contains a binary mask for the  $i$ th reliable phase region, and  $R(\chi)$  is a regularizer that imposes prior knowledge on the solution.

The first term in Equation (2) is the data consistency term that combines phase unwrapping, background phase removal using multiple SMV kernels and dipole inversion described by Equation (1). The term  $M_i(h_i * \Psi(\phi))$  represents the V-SHARP background phase removal technique, which employs multiple kernels with varying radii (49,50). By using the convolution theorem, we obtain the  $k$ -space form of Equation (2):

$$\min_{\chi} \frac{1}{2} \sum_i \left\| M_i F^{-1} H_i D F \chi - M_i F^{-1} H_i F \Psi(\phi) \right\|_2^2 + R(\chi) \quad [3]$$

where  $F$  is the discrete Fourier transform operator,  $D = \frac{1}{3} - \frac{k_z^2}{(k_x^2 + k_y^2 + k_z^2)}$  is the dipole kernel in  $k$ -space and  $H_i$  is the discrete Fourier transform of  $h_i$ . The second term in Equations (2) and (3) is the regularization term that imposes prior information on the solution. In this work, we propose two types of regularization  $R(\chi)$ : TV and second-order TGV. In the discrete setting, TV is defined as  $TV(\chi) = \|G\chi\|_1$ , where  $G$  is the 3D gradient operator. The second-order TGV operator is defined as  $TGV_{\alpha}^2(\chi) = \text{minimize}_{\nu} \alpha_1 \|G\chi - \nu\|_1 + \alpha_0 \|\varepsilon(\nu)\|_1$ , where  $\varepsilon$  is a symmetrized derivative as defined in ref. (26) and in the Appendix. Compared with quadratic smoothing (i.e.  $\ell_2$  penalty on the image gradients), both TV and TGV assign relatively less penalty to large degrees of signal variation. As a result, they mitigate noise and artifacts whilst preserving the edges in the signal. As opposed to TV, which only considers the first-order derivative, the second-order TGV also introduces the information about the second-order derivatives. It has been observed that the staircasing artifacts that often arise in TV-based reconstruction are mitigated in TGV-based reconstruction (26–28,51).

The improved models based on the more complicated data consistency term and TV/TGV regularization come at a cost of prolonged computation time. To address this, we propose an efficient solution to Equation (3) using ADMM with variable splitting in both data consistency and regularization terms. In addition, the special structures of the matrices in the model are also exploited. Consequently, the updates in all the subproblems can be carried out using closed-form solutions. [Please refer to the Appendix and the accompanying MATLAB code for implementation details.]

## EXPERIMENTAL DETAILS

Using two numerical brain phantoms, *in vivo* 3D echo planar imaging (EPI) data, *in vivo* multi-echo Wave-CAIPI data at 3 T and high-resolution *in vivo* Wave-CAIPI data at 7 T, we compared the performances of six different QSM methods with multiple SMV kernels:

- (i) SMV background filtering, followed by quadratic smoothing regularized dipole inversion (V-SHARP L2):

$$\min_{\chi} \left\| D F \chi - F \phi_{V-SHARP} \right\|_2^2 + \alpha \|G\chi\|_2^2$$

- (ii) SMV background filtering, followed by TV-regularized dipole inversion (V-SHARP TV):

$$\min_{\chi} \left\| D F \chi - F \phi_{V-SHARP} \right\|_2^2 + \alpha TV(\chi)$$

- (iii) SMV background filtering, followed by TGV-regularized dipole inversion (V-SHARP TGV):

$$\min_{\chi} \left\| D F \chi - F \phi_{V-SHARP} \right\|_2^2 + TGV_{\alpha}^2(\chi)$$

- (iv) single-step QSM with quadratic smoothing regularization (single-step L2):

$$\min_{\chi} \frac{1}{2} \sum_i \left\| M_i F^{-1} H_i D F \chi - M_i F^{-1} H_i F \Psi(\phi) \right\|_2^2 + \alpha \|G\chi\|_2^2$$

- (v) *proposed*: single-step QSM with TV regularization (single-step TV):

$$\min_{\chi} \frac{1}{2} \sum_i \left\| M_i F^{-1} H_i D F \chi - M_i F^{-1} H_i F \Psi(\phi) \right\|_2^2 + \alpha TV(\chi)$$

- (vi) *proposed*: single-step QSM with TGV regularization (single-step TGV):

$$\min_{\chi} \frac{1}{2} \sum_i \left\| M_i F^{-1} H_i D F \chi - M_i F^{-1} H_i F \Psi(\phi) \right\|_2^2 + TGV_{\alpha}^2(\chi).$$

For all the methods, the GRE phase was unwrapped using a Laplacian-based phase unwrapping algorithm (15,52). For the dataset with an anisotropic voxel size, the SMV kernels were scaled accordingly. For V-SHARP L2 and single-step L2, the MATLAB built-in preconditioned conjugate gradients (pcg) function was used with the residual tolerance of 0.1%. For the other four methods, ADMM was used with the stopping criterion that iterations were terminated when the solution change between consecutive iterations was less than 1%. For the TGV-based methods, we followed ref. (51) and set  $\alpha_0 : \alpha_1 = 2 : 1$  to reduce the number of regularization parameters that needed to be tuned. For the numerical phantoms, the regularization parameters were chosen to minimize the root-mean-square error (RMSE) of all the methods. For the *in vivo* data, regularization parameters were selected using the L-curve heuristic (24,53). All parameter values are reported in Table 1. A workstation with 16 Intel Xeon E5-2670 processors and 128 GB of memory was used in all experiments.

### Duke brain phantom

A numerical brain phantom based on the segmented Duke model (54) with a spatial resolution of  $1 \text{ mm}^3$  isotropic was generated with the following susceptibility values (in SI units): hippocampus, 0.05 ppm; hypothalamus, 0.05 ppm; medulla oblongata, 0.05 ppm; white matter,  $-0.03$  ppm; cerebellum,  $-0.0065$  ppm; pons,  $-0.0065$  ppm; thalamus,  $-0.0065$  ppm; midbrain,  $-0.0065$  ppm; cerebrospinal fluid (CSF), 0 ppm; skull,  $-2.1$  ppm. Additional magnetic susceptibility sources at 0.6 ppm were included to resemble subcutaneous fat without the

**Table 1.** Reconstruction parameters of each quantitative susceptibility mapping (QSM) method. For the numerical brain phantom, the reconstruction parameters were reported for the case in which we used five spherical mean value (SMV) kernels for all the methods. For three-dimensional echo planar imaging (3D EPI), the reconstruction parameters were reported for the case in which we used five SMV kernels for the single-step methods and 14 SMV kernels for the multi-step methods

Methods	Parameter	Duke brain phantom	Numerical brain phantom	3D EPI	ME Wave-CAIPI at 3 T	High-res. Wave-CAIPI at 7 T
V-SHARP L2	$\alpha$	$8 \times 10^{-3}$	$2 \times 10^{-2}$	$2.73 \times 10^{-2}$	$2.73 \times 10^{-2}$	$5.56 \times 10^{-2}$
V-SHARP TV	$\alpha$	$4 \times 10^{-4}$	$2 \times 10^{-4}$	$5.46 \times 10^{-3}$	$2.73 \times 10^{-4}$	$2.66 \times 10^{-2}$
V-SHARP TGV	$\mu$	$3 \times 10^{-2}$	$3 \times 10^{-2}$	$3 \times 10^{-3}$	$3 \times 10^{-3}$	$10^{-1}$
	$\alpha$	$3 \times 10^{-4}$	$2 \times 10^{-4}$	$4.36 \times 10^{-3}$	$2.73 \times 10^{-4}$	$2.66 \times 10^{-2}$
Single-step L2	$\mu_0 = \mu_1$	$3 \times 10^{-2}$	$3 \times 10^{-2}$	$3 \times 10^{-3}$	$3 \times 10^{-3}$	$10^{-1}$
	$\alpha$	$3 \times 10^{-3}$	$3 \times 10^{-4}$	$2.66 \times 10^{-2}$	$2.09 \times 10^{-2}$	$6.80 \times 10^{-3}$
Single-step TV	$\alpha$	$2 \times 10^{-4}$	$7 \times 10^{-5}$	$5.46 \times 10^{-3}$	$2.69 \times 10^{-4}$	$7.00 \times 10^{-3}$
	$\mu_0 = \mu_1$	$3 \times 10^{-2}$	$3 \times 10^{-2}$	$10^{-1}$	$10^{-1}$	$10^{-1}$
Single-step TGV	$\alpha_0$	$3 \times 10^{-4}$	$6 \times 10^{-5}$	$5.46 \times 10^{-3}$	$2.69 \times 10^{-4}$	$7.00 \times 10^{-3}$
	$\mu_0 = \mu_1 = \mu_2$	$3 \times 10^{-2}$	$3 \times 10^{-2}$	$10^{-1}$	$10^{-1}$	$10^{-1}$

CAIPI, controlled aliasing in parallel imaging; ME, multi-echo; SHARP, sophisticated harmonic artifact reduction for phase data; TGV, total generalized variation; TV, total variation.

chemical shift effect. In addition, magnetic susceptibility sources at 9.2 ppm were included within the head to mimic internal air in the nasal cavity and ear canal. The resulting phantom was convolved with the dipole kernel to generate the field map, and Gaussian white noise was then added to obtain an RMSE of 2.4% with respect to the noise-free field map. For all methods, background removal was performed using five SMV kernels with radii ranging from 1 voxel to 5 voxels, with a step size of 1 voxel.

For the multi-step methods (V-SHARP L2, V-SHARP TV and V-SHARP TGV), we also reconstructed the susceptibility map from the background-free tissue phase to demonstrate that an error from the background field removal step propagates into the dipole inversion.

### Numerical brain phantom

A numerical brain phantom with a resolution of  $0.94 \times 0.94 \times 1.5 \text{ mm}^3$  was adapted from refs. (28,55) with the following susceptibility values (in SI units): CSF, 0 ppm; globus pallidus, 0.19 ppm; putamen, 0.09 ppm; red nucleus, 0.07 ppm; substantia nigra, 0.09 ppm; dentate nucleus, 0.09 ppm; caudate nucleus, 0.09 ppm; cortical gray matter, 0.05 ppm. With this set-up, the white matter structures had magnetic susceptibility values between  $-0.03$  ppm and  $-0.01$  ppm. In addition to the susceptibility sources inside the brain, two additional susceptibility sources were positioned in the region in close proximity to the brain to provide background field intensity and pattern that were similar to those appearing in the *in vivo* EPI dataset (28). The resulting phantom was convolved with the dipole kernel to generate the field map, and Gaussian white noise was then added to obtain an RMSE of 2.4% with respect to the noise-free field map. Different numbers of SMV kernels with a maximum radius size ranging from 1 voxel to 8 voxels, and with a step size of 1 voxel, were tested to demonstrate the effect of the kernel size on the reconstructed susceptibility map.

### 3D EPI

Four-average data were acquired from a healthy volunteer (32-year-old man) with written informed consent using a 3D EPI

sequence (56) at 3 T (TimTrio, Siemens Healthcare, Erlangen, Germany) in 57 s. The imaging parameters were as follows: field of view (FOV),  $230 \text{ mm} \times 230 \text{ mm} \times 176 \text{ mm}$ ; spatial resolution,  $1 \text{ mm}^3$  isotropic; TR = 69 ms; TE = 21 ms; GRAPPA acceleration factor, 4; partial Fourier along the primary phase-encoding direction, 75%; number of receiver coils, 32. Based on the results obtained from the numerical brain phantom, we observed that the use of five SMV kernels for the single-step methods gave a good balance between the reduction in RMSE and the increase in reconstruction time. Consequently, for the single-step methods, five SMV kernels with radii ranging from 1 voxel to 5 voxels, and with a step size of 1 voxel, were used. Similarly, we observed that the use of 14 SMV kernels also gave a good tradeoff for the multi-step methods (results not shown); therefore, we employed 14 SMV kernels with radii ranging from 1 voxel to 14 voxels, and with a step size of 1 voxel, for the multi-step methods.

As an additional comparison, we also reconstructed the susceptibility map using the multi-step methods with five SMV kernels to demonstrate the effect of using different reconstruction methods with the same number of SMV kernels for this *in vivo* dataset.

### Multi-echo Wave-CAIPI at 3 T

Wave-CAIPI is a parallel imaging technique that allows highly accelerated acquisition with minimal *g*-factor noise amplification penalty (37,57). This is achieved through a helical *k*-space trajectory that increases the distance between the aliasing voxels in subsampled acquisitions, thus improving the variation in the coil sensitivity profiles and providing better parallel imaging capability. This acquisition strategy has so far been applied to single-echo 3D GRE imaging to achieve nine-fold acceleration with near-perfect *g*-factor performance (37). Although Wave-CAIPI largely mitigates the *g*-factor noise amplification penalty caused by parallel imaging reconstruction, the intrinsic  $\sqrt{R}$  penalty on SNR still hampers the achievable image quality. At nine-fold acceleration ( $R = 9$ ), this incurs a three-fold reduction in the SNR, which would be especially challenging for high-resolution imaging. To mitigate this intrinsic SNR penalty, herein we have extended the Wave-CAIPI acquisition to sample

multiple echoes within each TR, thus increasing the effective signal averaging time and boosting the SNR. As detailed below, we also propose a rapid acquisition and processing pipeline for coil sensitivity estimation to provide phase-sensitive, high-quality parallel imaging reconstruction.

### Coil sensitivity estimation

Accurate estimation of coil sensitivities is crucial for successful parallel imaging at high acceleration factors whilst preserving the object phase. ESPIRiT provides high-fidelity coil sensitivities by estimating the coil profiles that are implicitly used in autocalibrating  $k$ -space-based parallel imaging methods (39). The phase of the sensitivities, however, is taken to be relative to the first channel (i.e. the first ESPIRiT coil profile which has zero phase). This presents a challenge as the fringe lines, also known as phase singularities, present in the first channel will propagate to the other channels, which will then reflect to the coil combined image. To address this, we employ the virtual body coil concept and obtain a reference channel by applying singular value decomposition (SVD) coil compression (38). At 3 T, the dominant singular vector (i.e. the compressed channel with the largest signal) is observed to have slowly varying phase and can replace the body coil acquisition as phase reference. By inputting the dominant singular vector to ESPIRiT as the first channel, we thus achieve automated, phase-sensitive coil sensitivity estimation. At 7 T, the wavelength of coil sensitivity patterns is on the order of the subject's head, and the interaction between the magnetic field and the subject is much higher. This leads to more complicated coil sensitivity profiles. As such, the dominant singular vector may no longer be spatially smooth and phase singularities could become a concern at ultra-high field.

For calibration, we use a low-resolution ( $k_y \times k_x = 30 \times 30$ ) 3D GRE acquisition with short TE/TR=2/3.5 ms. This requires less than 4 s of scan time, which is then SVD compressed to 21 channels whilst the compression error remains below 1%. This pipeline is depicted in Fig. 1. The same SVD matrix is also applied to the high-resolution undersampled Wave-CAIPI data for coil compression.

### Multi-echo Wave-CAIPI acquisition and reconstruction

$R=3 \times 3$ -fold accelerated data were acquired from a healthy volunteer (33-year-old man) with written informed consent using multi-echo Wave-CAIPI at 3 T (TimTrio, Siemens Healthcare) in

110 s. Imaging parameters were as follows: FOV, 256 mm  $\times$  192 mm  $\times$  120 mm; spatial resolution, 1 mm<sup>3</sup> isotropic; TR=43 ms; TEs=9/22/35 ms; bandwidth, 100 Hz/pixel; number of receiver coils, 32. The undersampled coil-compressed Wave-CAIPI data were reconstructed using generalized SENSE (37,58) with ESPIRiT coil sensitivities. The magnitude images from the three echoes were merged with root-mean-square combination, whereas the phase images were unwrapped, normalized by their TEs and then averaged for improved SNR (Fig. 2). The combined frequency map was then processed by the QSM algorithms.

### QSM for multi-echo Wave-CAIPI

For the single-step methods, five SMV kernels with radii ranging from 1 voxel to 5 voxels, and with a step size of 1 voxel, were used. For the multi-step methods, background field removal was performed using 14 SMV kernels with radii ranging from 1 voxel to 14 voxels, with a step size of 1 voxel.

### High-resolution Wave-CAIPI at 7 T

To compare the QSM reconstructions on high-resolution 3D GRE data, one healthy volunteer (32-year-old man) underwent MRI at 7 T (Siemens Magnetom) using a 32-channel custom receive array. The imaging protocol included the single-echo Wave-CAIPI sequence (TE/TR=20/30 ms; 0.5 mm<sup>3</sup> isotropic resolution; bandwidth, 100 Hz/pixel; matrix size, 384  $\times$  512  $\times$  240) with  $R=3 \times 3$ , which resulted in a total acquisition time of 5 min. For the single-step methods, five SMV kernels with radii ranging from 1 voxel to 5 voxels, and with a step size of 1 voxel, were used. For the multi-step methods, background removal was performed using 14 SMV kernels with radii ranging from 1 voxel to 14 voxels, with a step size of 1 voxel.

## RESULTS

Figures 3–8 and S1–S4 show the reconstruction results obtained from the six different QSM algorithms. The reconstruction times are reported in Table 2. Although it has been observed that the staircasing artifacts that often arise in TV-based reconstructions are mitigated in TGV-based reconstructions in several applications (26–28,51), we observed that the reconstruction quality of the proposed single-step TV and single-step TGV methods was comparable in our experiments, as shown in the figures (especially in Fig. S4).

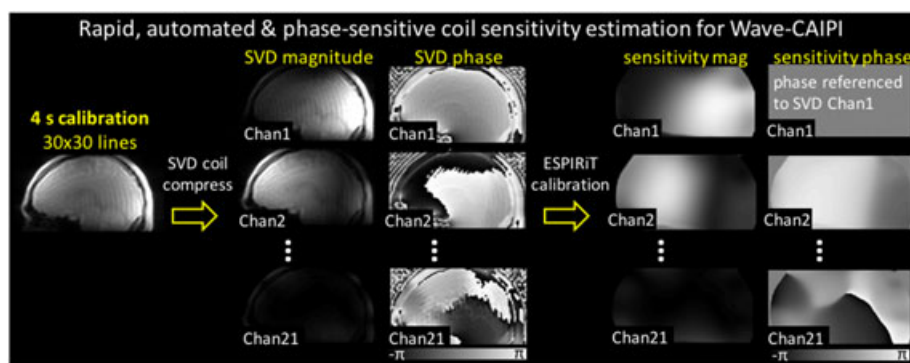


**Figure 1.** The pipeline of the proposed rapid, automated and phase-sensitive coil sensitivity estimation for Wave-CAIPI (controlled aliasing in parallel imaging). SVD, singular value decomposition.

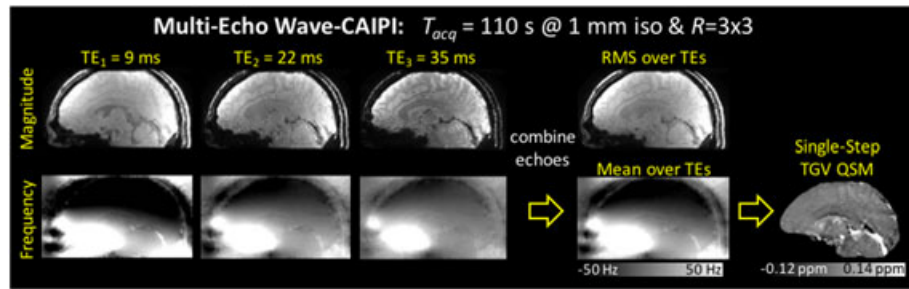


**Figure 2.** Multi-echo Wave-CAIPI (controlled aliasing in parallel imaging). The unwrapped phase images were normalized by their TEs and averaged for improved signal-to-noise ratio (SNR). The resulting combined phase was then processed by the quantitative susceptibility mapping (QSM) algorithms. RMS, root mean square; TGV, total generalized variation.

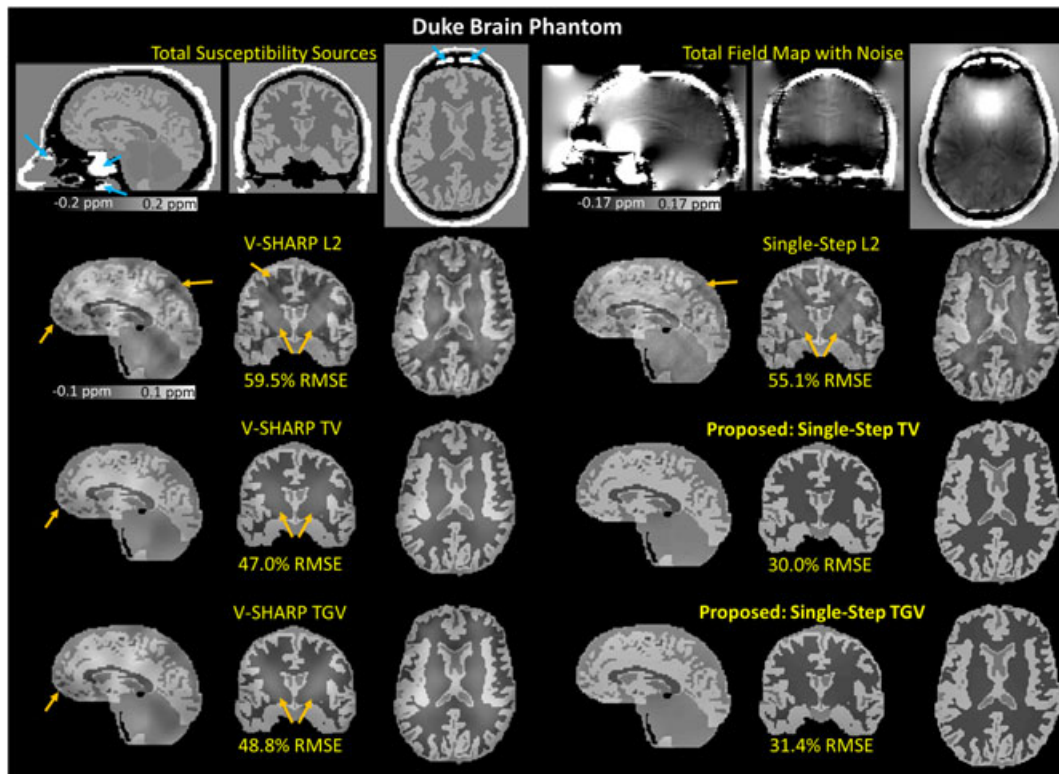


**Figure 3.** Duke brain phantom. The reconstructed magnetic susceptibility maps obtained from six different quantitative susceptibility mapping (QSM) algorithms [five spherical mean value (SMV) kernels] with their corresponding root-mean-square errors (RMSEs). The blue arrows indicate the magnetic susceptibility sources (9.2 ppm) that mimic internal air in the nasal cavity and ear canal. The orange arrows indicate the apparent remaining dipole artifacts and background phase contamination. SHARP, sophisticated harmonic artifact reduction for phase data; TV, total variation; TGV, total generalized variation.

### Duke brain phantom

Using five SMV kernels, the RMSEs of the reconstructed susceptibility maps with respect to the true susceptibility distribution were 59.5% for V-SHARP L2, 47.0% for V-SHARP TV, 48.8% for V-SHARP TGV, 55.1% for single-step L2, 30.0% for single-step TV and 31.4% for single-step TGV. As shown in Figs 3 and S1, single-step TV and single-step TGV better mitigated the background phase contamination and dipole artifacts (indicated by the orange arrows) compared with the other methods.

The application of V-SHARP filtering to the total phase, which had contributions from both underlying tissue and background components, resulted in a filtered phase that had 49.5% RMSE

with respect to the underlying tissue phase. By performing the dipole inversions on the V-SHARP filtered phase, we obtained susceptibility maps with RMSEs of 59.5% using quadratic smoothing, 47.0% using TV and 48.8% using TGV regularizations, with respect to the underlying susceptibility map. Instead of using the V-SHARP filtered phase, we also performed the dipole inversions on the underlying background-free tissue phase. The RMSEs of the reconstructed susceptibility maps were 19.4%, 5.9% and 5.9% using quadratic smoothing, TV- and TGV-regularized dipole inversions, respectively. In this case, the RMSEs of the reconstructed susceptibility maps were much lower than those obtained from the methods that involved V-

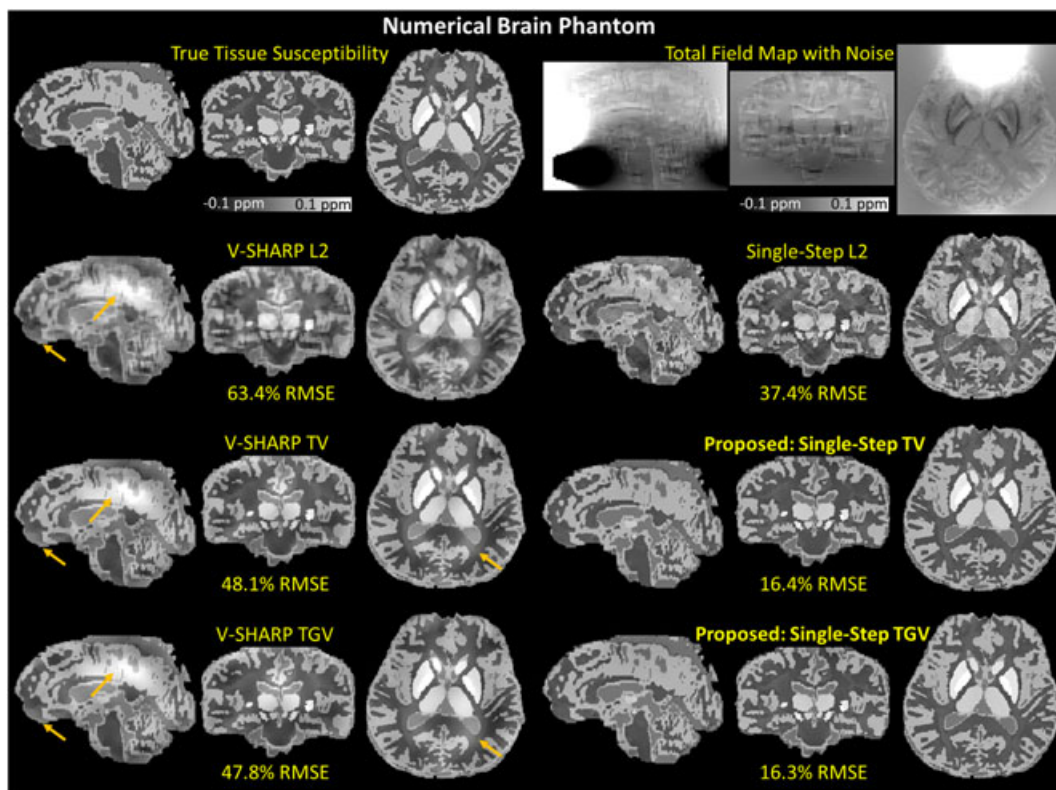


**Figure 4.** Numerical brain phantom. The reconstructed magnetic susceptibility maps obtained from six different quantitative susceptibility mapping (QSM) algorithms [five spherical mean value (SMV) kernels] with their corresponding root-mean-square errors (RMSEs). Single-step total variation (TV) and single-step total generalized variation (TGV) better mitigated the background phase contamination and dipole artifacts (indicated by the orange arrows) compared with the other methods. SHARP, sophisticated harmonic artifact reduction for phase data.

#### Numerical Brain Phantom: RMSE vs number of SMV kernels

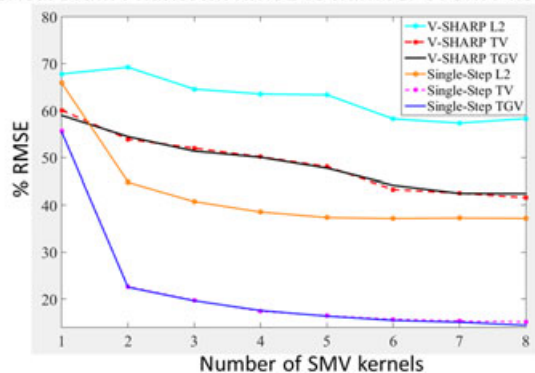


**Figure 5.** Numerical brain phantom. Root-mean-square errors (RMSEs) of the reconstructed magnetic susceptibility maps obtained from six different quantitative susceptibility mapping (QSM) algorithms. SHARP, sophisticated harmonic artifact reduction for phase data; SMV, spherical mean value; TV, total variation; TGV, total generalized variation.

SHARP filtering. With this comparison, we have demonstrated that an error from the background field removal step propagated into the dipole inversion step.

#### Numerical brain phantom

Using five SMV kernels, the RMSEs of the reconstructed susceptibility maps with respect to the true susceptibility distribution were 63.4% for V-SHARP L2, 48.1% for V-SHARP TV, 47.8% for

V-SHARP TGV, 37.4% for single-step L2, 16.4% for single-step TV and 16.3% for single-step TGV. The RMSEs for specific regions with respect to the underlying magnetic susceptibility values are reported in Table 3. As shown in Figs 4 and S2, single-step TV and single-step TGV better mitigated the background phase contamination and dipole artifacts (indicated by the orange arrows) compared with the other methods. As shown in Fig. 5 and listed in Table 3, both single-step TV and single-step TGV yielded lower RMSEs compared with the other methods with the same number of SMV kernels.

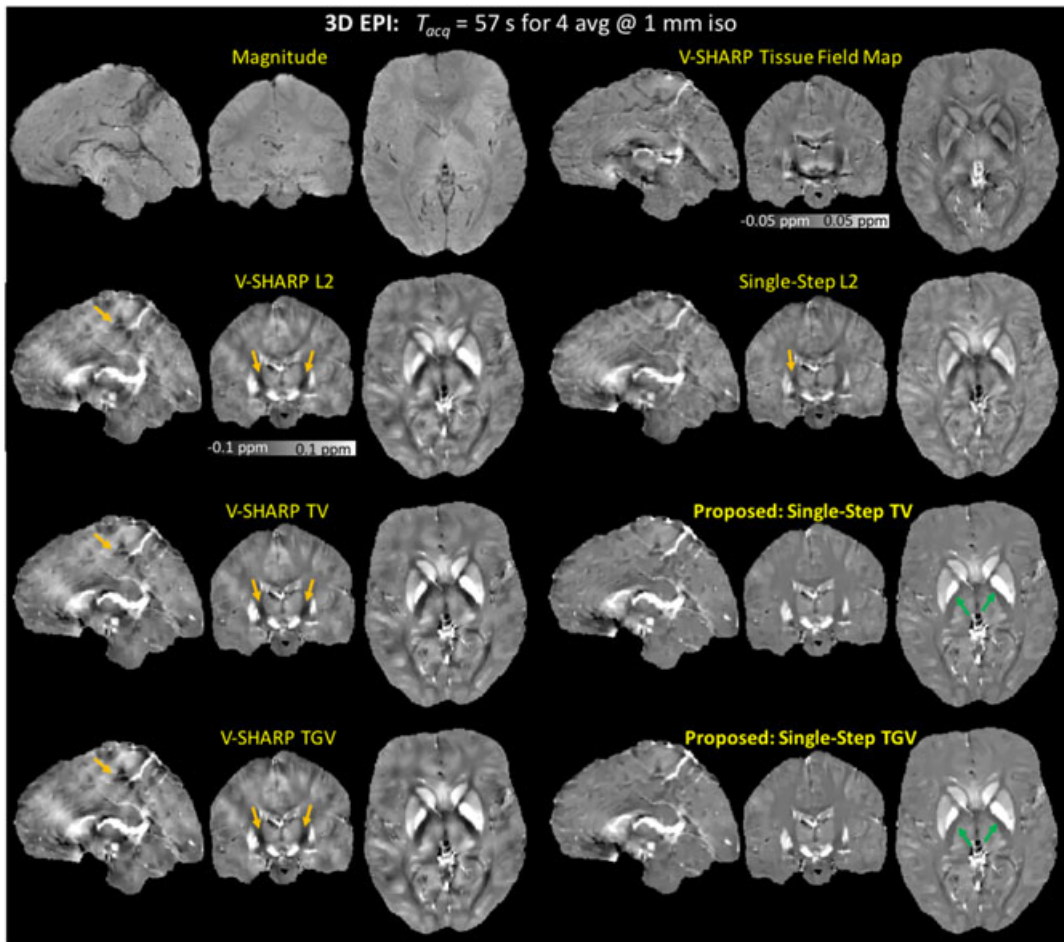
#### 3D EPI

Figure 6 shows the reconstructed susceptibility maps obtained from the multi-step (14 SMV kernels) and single-step (five SMV kernels) methods. Single-step TV and single-step TGV mitigated the dipole artifacts (indicated by the orange arrows) more successfully. Nevertheless, the artifact mitigation obtained from the proposed methods came at a cost of reduced contrast between white matter and gray matter (indicated by the green arrows).

Figure S3 shows the results of an additional comparison where we reconstructed the susceptibility maps using all the methods with the same number of SMV kernels (five SMV kernels).

#### Multi-echo Wave-CAIPI at 3 T

As shown in Fig. 7, the reconstructed susceptibility map obtained using the proposed methods had the lowest level of



**Figure 6.** Three-dimensional echo planar imaging (3D EPI). The reconstructed magnetic susceptibility maps obtained from the multi-step [14 spherical mean value (SMV) kernels] and single-step (five SMV kernels) methods. Single-step total variation (TV) and single-step total generalized variation (TGV) mitigated the dipole artifacts (indicated by the orange arrows) more successfully, but with reduced contrast between white matter and gray matter (indicated by the green arrows). SHARP, sophisticated harmonic artifact reduction for phase data.

dipole artifacts (indicated by the orange arrows), but with reduced contrast between white matter and gray matter (indicated by the green arrows). Compared with single-step L2, the proposed methods with the same SMV kernel sizes alleviated the  $B_0$  artifacts in the temporal lobes, as indicated by the pink arrows in the single-step L2 reconstructed susceptibility map.

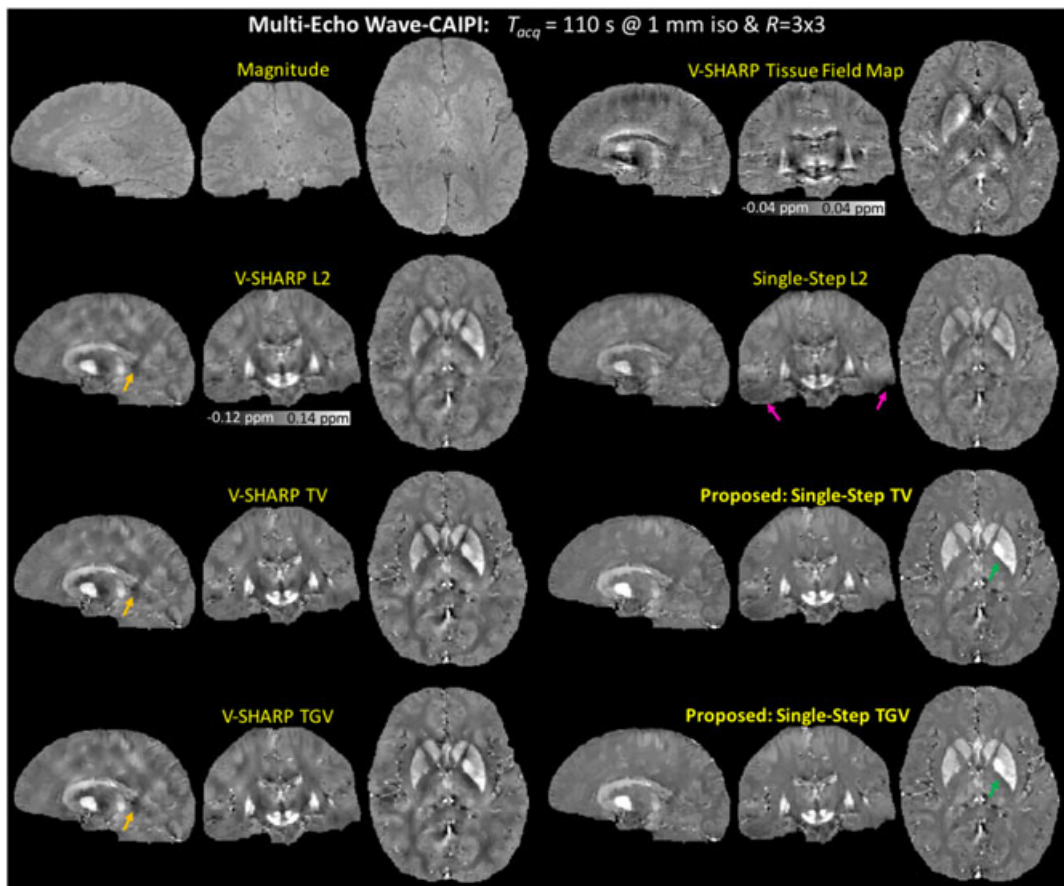
### High-resolution Wave-CAIPI at 7 T

Figure 8 shows the reconstructed magnetic susceptibility maps of the high-resolution *in vivo* Wave-CAIPI data at 7 T. The proposed methods alleviated the artifacts that were apparent in the other four methods, as indicated by the orange arrows. The susceptibility maps reconstructed using the multi-step methods and the single-step methods have a different visual appearance. Compared with the multi-step methods, the proposed methods removed the artifacts whilst preserving small details, such as edges. As indicated by the pink arrow in the V-SHARP tissue field map, the cortical regions became blurred after the dipole inversion in the multi-step methods. Compared with single-step L2, the proposed methods had fewer streaking artifacts.

## DISCUSSION

In this work, the background phase was removed by exploiting the harmonic mean value property, which involves the convolution of the total phase with SMV kernels (17). An SMV kernel with large radius is typically desirable because it provides a better approximation of the radially symmetric SMV kernel as it suffers less from discretization effects. Nevertheless, as the voxels close to the object boundary have contributions from regions with no detectable MRI signal in the convolution process, the size of the trustable region becomes smaller when a larger SMV kernel is employed. Although a smaller SMV kernel could be used to enlarge the trustable region, the small SMV kernel would cause a large residual phase error amplification, which reduces the background phase removal accuracy within the trustable region (49). In order to take advantage of larger SMV kernels without significantly shrinking the trustable region, SMV kernels with different radii can be employed (49). By using multiple SMV kernels with different radii, the trustable region is enlarged by the smaller SMV kernels, and the background phase removal accuracy within the trustable region is improved towards the center of the brain because larger SMV kernels are used near the center.





**Figure 7.** Multi-echo Wave-CAIPI (controlled aliasing in parallel imaging). The reconstructed magnetic susceptibility maps obtained from six different quantitative susceptibility mapping (QSM) algorithms. The proposed methods had the lowest level of dipole artifacts (indicated by the orange arrows), but with reduced contrast between white matter and gray matter (indicated by the green arrows). Compared with single-step L2, the proposed methods with the same spherical mean value (SMV) kernel sizes alleviated the  $B_0$  artifacts in the temporal lobes in the single-step L2 reconstructed susceptibility map (pink arrows). SHARP, sophisticated harmonic artifact reduction for phase data; TV, total variation; TGV, total generalized variation.

By incorporating the use of multiple SMV kernels into our models and estimating the underlying susceptibility distribution in a single step, potential error propagation from one step to subsequent steps was prevented. Furthermore, the proposed methods use TV and TGV regularizations, which provide more natural signal models than obtained by quadratic smoothing. In particular, TV promotes a piecewise-constant solution, and the second-order TGV promotes a piecewise-smooth solution. Consequently, the proposed methods successfully suppress dipole artifacts whilst preserving the edges in the signal. Because the proposed methods benefit from the combination of multiple SMV kernels, single-step reconstruction and TV/TGV regularization, they give reconstructed susceptibility maps that have the lowest level of dipole artifacts compared with the other methods evaluated in this work. As demonstrated using numerical and *in vivo* experiments, the proposed single-step methods mitigate dipole artifacts more successfully than the methods that involve sequential SMV filtering followed by dipole inversion. As shown in the *in vivo* multi-echo Wave-CAIPI result, the proposed methods also remove the background phase contamination more effectively, especially in regions with large  $B_0$  inhomogeneity, compared with the single-step QSM with quadratic smoothing regularization.

The optimization problems associated with the proposed methods were efficiently solved using ADMM with variable splitting to decompose the original problem into smaller ones that

can be solved easily. We applied variable splitting not only to the regularization terms, but also to the data consistency term (59), so that the subproblems were further simplified. Moreover, by recognizing the special structures of the matrices in our problem, all the updates for the subproblems were performed using the analytical formulae described in the Appendix.

This work also introduced multi-echo Wave-CAIPI, which is an efficient sequence that fully utilizes TR for data sampling, hence boosting the SNR in the GRE phase and magnitude images. Although Wave-CAIPI substantially mitigates the  $g$ -factor noise amplification penalty as a result of parallel imaging reconstruction, the  $\sqrt{R}$  penalty caused by  $k$ -space subsampling intrinsically reduces the SNR of the acquired data. Multi-echo Wave-CAIPI mitigates this intrinsic SNR penalty by continuously sampling the data during the entire acquisition window. The magnitude images are combined by taking the RMS over the echoes, providing SNR benefit that can be useful for susceptibility-weighted imaging (60). In addition, the frequency maps are computed by unwrapping the raw phase of each echo, normalizing by their TEs and averaging to improve SNR.

Combination of the channels in an array coil is an important step for the imaging of phase and susceptibility contrast. The estimated coil sensitivities used in the combination should not include the phase of the imaged object, otherwise the combined phase will be severely underestimated. The sensitivity estimates

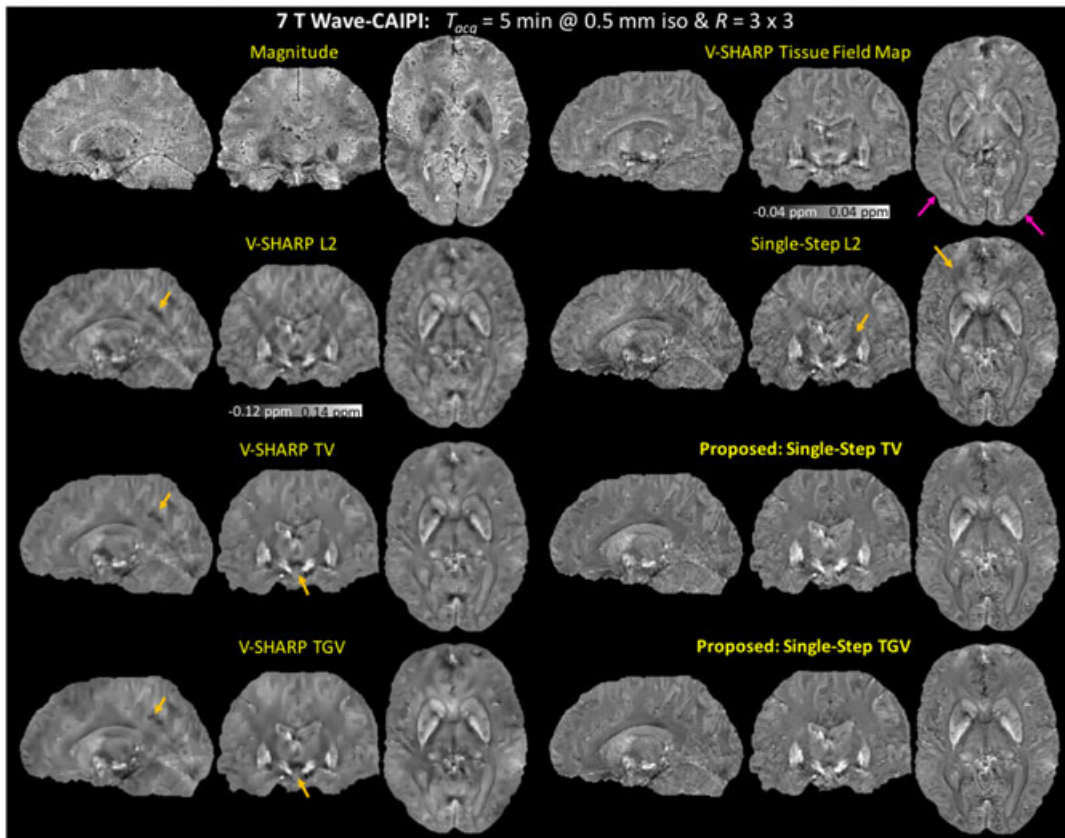


**Figure 8.** High-resolution Wave-CAIPI (controlled aliasing in parallel imaging) at 7 T. The proposed methods alleviated the artifacts that were apparent in the other four methods as indicated by the orange arrows. As indicated by the pink arrow in the V-SHARP tissue field map, the cortical regions became blurred after the dipole inversion in the multi-step methods. SHARP, sophisticated harmonic artifact reduction for phase data; TV, total variation; TGV, total generalized variation.

**Table 2.** Reconstruction times of each quantitative susceptibility mapping (QSM) method. For the numerical brain phantom, the reconstruction times were reported for the case in which we used five spherical mean value (SMV) kernels for all the methods. For three-dimensional echo planar imaging (3D EPI), the reconstruction times were reported for the case in which we used five SMV kernels for the single-step methods and 14 SMV kernels for the multi-step methods

Methods	Reconstruction time (s)				
	Duke brain phantom	Numerical brain phantom	3D EPI	ME Wave-CAIPI at 3 T	High-res. Wave-CAIPI at 7 T
V-SHARP L2	0.2	0.2	0.2	0.2	0.8
V-SHARP TV	9.5	6.0	13.5	10.3	29.9
V-SHARP TGV	41.3	50.5	54.9	75.0	158.1
Single-step L2	111.3	101.8	25.1	30.8	205.3
Single-step TV	127.8	105.8	82.9	80.5	350.6
Single-step TGV	243.7	189.3	258.3	200.6	870.7

CAIPI, controlled aliasing in parallel imaging; ME, multi-echo; SHARP, sophisticated harmonic artifact reduction for phase data; TGV, total generalized variation; TV, total variation.

also need to capture the fringe lines in order to prevent their propagation to the combined phase image. An effective way to address both of these issues is to acquire additional reference data with slowly varying phase in the birdcage mode or with the body coil (58). Alternatively, multi-echo reference images can be collected to estimate the phase offset of the sensitivities (31,61). In this work, we used a 4-s, low-resolution, single-echo

calibration acquisition with the array coil for calibration. As demonstrated in ref. (38), the dominant singular vector of SVD coil compression can serve as a virtual body coil for phase reference. As this is a linear combination of all channels, it will still contain the object phase, whilst being sufficiently smooth to exclude phase singularities at 3 T. At ultra-high field, where the coil sensitivity profiles become more complicated, the smooth

**Table 3.** Numerical brain phantom. Root-mean-square errors (RMSEs, %) in specific regions of the reconstructed magnetic susceptibility maps [five spherical mean value (SMV) kernels] with respect to the underlying susceptibility values

Methods ROIs	V-SHARP L2	V-SHARP TV	V-SHARP TGV	Single-step L2	Single-step TV	Single-step TGV
CSF(0 ppm)	227.3	188.6	188.5	162.7	55.7	55.7
Globus pallidus(0.19 ppm)	24.2	6.6	4.1	15.8	2	1.8
Putamen, substantia nigra, dentate nucleus and caudate nucleus(0.09 ppm)	32.9	14.6	13.3	19.0	4.7	4.4
Red nucleus(0.07 ppm)	27.9	19.5	21.8	19.4	3.8	4.0
Cortical gray matter(0.05 ppm)	60.1	41.6	41.1	34.1	14.7	15.0
White matter(-0.03 to -0.01 ppm)	67.5	54.8	54.7	39.3	18.8	18.4

CSF, cerebrospinal fluid; ROI, region of interest; SHARP, sophisticated harmonic artifact reduction for phase data; TGV, total generalized variation; TV, total variation.

assumption may no longer hold, and the virtual body coil may contain singularities. For automated estimation of sensitivities, we employed ESPIRiT (39), which uses the first channel as phase reference. As such, when the dominant singular vector of the SVD compression is arranged to be the first channel, it acts as a virtual body coil reference during ESPIRiT reconstruction. Processing the rapid calibration data with ESPIRiT and the SVD virtual coil concept thus allows the phase-sensitive estimation of coil sensitivities.

### Extensions and limitations

Although the combination of ADMM and variable splitting enables an efficient solver for the regularized optimization, more augmented Lagrangian parameters corresponding to the consensus constraints are introduced in the proposed algorithms. To simplify parameter selection, we chose the same value for all Lagrangian parameters of the proposed methods. For single-step TGV, we fixed the ratio between the regularization parameters  $\alpha_0 : \alpha_1$  to 2 : 1. Consequently, we were left with two parameters in the proposed methods, one for regularization and one for the consensus constraints that needed to be tuned. For the numerical simulations, these parameters were chosen to minimize the RMSE. For the *in vivo* experiments, all the augmented Lagrangian parameters of the proposed methods were set to 0.1, and the regularization parameter was chosen using the L-curve criterion.

As described in the Appendix, the proposed algorithm allows the parallel updates of the variables associated with each subproblem. However, the current implementation uses the sequential updates for the  $z_{2,i}$  values, and so the reconstruction time could be further reduced by using the parallel updates for all the subproblems. The improvement in the computation time could be used to increase the number of SMV kernels by including even larger filter diameters, which would lead to improved background phase removal. A further algorithmic advancement could involve the use of an exponential signal model rather than a linear system in the single-step reconstruction, which enables high-quality susceptibility mapping even when a crude brain mask is employed (34).

For multi-echo Wave-CAIPI acquisition, a model-based approach that jointly estimates magnitude and frequency components across the echoes could provide improved reconstruction. This would entail a signal model comprising the product of a complex amplitude and a complex exponential per

voxel. These two unknowns could then be estimated from subsampled  $k-t$  space using model-based reconstruction similar to that of ref. (62). As the number of echoes acquired increases, the accuracy of the model fit would improve, as it would be easier to estimate two unknowns from several data points. This could potentially improve parallel imaging quality and could enable alternative sampling schemes in which each echo samples a different  $k$ -space location.

### CONCLUSION

In this work, we proposed novel QSM methods that unify SMV filtering with multiple kernels and TV/TGV regularization within a single step. Using ADMM with variable splitting and exploiting special structures of the matrices in the models, we developed efficient algorithms that involve analytical solutions for all of the optimization steps. As demonstrated using the numerical phantoms and *in vivo* datasets, the proposed methods better mitigated the dipole artifacts compared with other QSM methods evaluated. We also introduced an automated sensitivity estimation scheme that relies on a rapid 4-s acquisition for phase-sensitive coil combination. This permitted high-quality parallel imaging with Wave-CAIPI, which was extended to acquire multiple echoes for improved SNR efficiency. The combination of multi-echo Wave-CAIPI and single-step QSM with TV/TGV regularization thus enabled high-quality susceptibility mapping with efficient acquisition and reconstruction.

### ACKNOWLEDGEMENTS

The authors thank Susie Y. Huang, Michael Khalil, Salil Soman and Jeffrey Stout for helpful discussions. Grant support was provided by the National Institutes of Health (NIH): R01EB017219, P41EB015896, 1U01MH093765, R24MH106096 and 1R01EB017337-01.

### REFERENCES

1. Duyn J, van Gelderen P, Tie-Qiang L, de Zwart JA, Koretsky AP, Fukunaga M. High-field MRI of brain cortical substructure based on signal phase. *Proc. Natl. Acad. Sci.* 2007; 104: 11 796–11 801.
2. Liu C, Li W, Tong KA, Yeom KW, Kuzminski S. Susceptibility-weighted imaging and quantitative susceptibility mapping in the brain. *J. Magn. Reson. Imaging* 2015; 42: 23–41.

3. Wang Y, Liu T. Quantitative susceptibility mapping (QSM): decoding MRI data for a tissue magnetic biomarker. *Magn. Reson. Med.* 2015; 73: 82–101.
4. Marques JP, Bowtell R. Application of a Fourier-based method for rapid calculation of field inhomogeneity due to spatial variation of magnetic susceptibility. *Concepts Magn. Reson. Part B: Magn. Reson. Eng.* 2005; 25B: 65–78.
5. Deistung A, Schäfer A, Schweser F, Biedermann U, Turner R, Reichenbach JR. Toward in vivo histology: a comparison of quantitative susceptibility mapping (QSM) with magnitude-, phase-, and R2\*-imaging at ultra-high magnetic field strength. *Neuroimage* 2013; 65: 299–314.
6. Argyridis I, Li W, Johnson GA, Liu C. Quantitative magnetic susceptibility of the developing mouse brain reveals microstructural changes in the white matter. *Neuroimage* 2014; 88: 134–142.
7. Li W, Wu B, Batrachenko A, Bancroft-Wu V, Morey RA, Shashi V, Langkammer C, De Bellis MD, Ropele S, Song AW, Liu C. Differential developmental trajectories of magnetic susceptibility in human brain gray and white matter over the lifespan. *Hum. Brain Mapp.* 2014; 35: 2698–2713.
8. Bilgic B, Pfefferbaum A, Rohlfing T, Sullivan EV, Adalsteinsson E. MRI estimates of brain iron concentration in normal aging using quantitative susceptibility mapping. *Neuroimage* 2012; 59: 2625–2635.
9. Acosta-Cabronero J, Williams G, Cardenas-Blanco A, Arnold RJ, Lupson V, Nestor PJ. In vivo quantitative susceptibility mapping (QSM) in Alzheimer's disease. *PLoS One* 2013; 8: e81093
10. Langkammer C, Liu T, Khalil M, Enzinger C, Jehna M, Fuchs S, Fazekas F, Wang Y, Ropele S. Quantitative susceptibility mapping in multiple sclerosis. *Radiology* 2013; 267: 551–559.
11. Wisnieff C, Ramanan S, Olesik J, Gauthier S, Wang Y, Pitt D. Quantitative susceptibility mapping (QSM) of white matter multiple sclerosis lesions: interpreting positive susceptibility and the presence of iron. *Magn. Reson. Med.* 2015; 74: 564–570.
12. Fan AP, Benner T, Bolar DS, Rosen BR, Adalsteinsson E. Phase-based regional oxygen metabolism (PROM) using MRI. *Magn. Reson. Med.* 2012; 67: 669–678.
13. Fan AP, Evans KC, Stout JN, Rosen BR, Adalsteinsson E. Regional quantification of cerebral venous oxygenation from MRI susceptibility during hypercapnia. *Neuroimage* 2015; 104: 146–155.
14. Fan AP, Bilgic B, Gagnon L, Witzel T, Bhat H, Rosen BR, Adalsteinsson E. Quantitative oxygenation venography from MRI phase. *Magn. Reson. Med.* 2013; 72: 149–159.
15. Li W, Wu B, Liu C. Quantitative susceptibility mapping of human brain reflects spatial variation in tissue composition. *Neuroimage* 2011; 55: 1645–1656.
16. Witoszynskij S, Rauscher A, Barth M. Phase unwrapping of MR images using  $\phi$ UN—A fast and robust region growing algorithm. *Med. Image Anal.* 2009; 13: 257–268.
17. Schweser F, Deistung A, Lehr BW, Reichenbach JR. Quantitative imaging of intrinsic magnetic tissue properties using MRI signal phase: an approach to in vivo brain iron metabolism? *Neuroimage* 2011; 54: 2789–2807.
18. Liu T, Khalidov I, de Rochefort L, Spincemaille P, Liu J, Tsiouris AJ, Wang Y. A novel background field removal method for MRI using projection onto dipole fields (PDF). *NMR Biomed.* 2011; 24: 1129–1136.
19. De Rochefort L, Liu T, Kressler B, Liu J, Spincemaille P, Lebon V, Wu J, Wang Y. Quantitative susceptibility map reconstruction from MR phase data using bayesian regularization: validation and application to brain imaging. *Magn. Reson. Med.* 2010; 63: 194–206.
20. Bilgic B, Chatnuntaweck I, Fan A, Setsompop K, Cauley S, Wald L, Adalsteinsson E. Fast image reconstruction with L2-regularization. *J. Magn. Reson. Imaging* 2014; 40: 181–191.
21. Liu T, Xu W, Spincemaille P, Avestimehr AS, Wang Y. Accuracy of the morphology enabled dipole inversion (MEDI) algorithm for quantitative susceptibility mapping in MRI. *IEEE Trans. Med. Imaging* 2012; 31: 816–824.
22. Liu T, Liu J, de Rochefort L, Spincemaille P, Khalidov I, Ledoux JR, Wang Y. Morphology enabled dipole inversion (MEDI) from a single-angle acquisition: comparison with COSMOS in human brain imaging. *Magn. Reson. Med.* 2011; 66: 777–783.
23. Liu J, Liu T, de Rochefort L, Ledoux J, Khalidov I, Chen W, Tsiouris AJ, Wisnieff C, Spincemaille P, Prince MR, Wang Y. Morphology enabled dipole inversion for quantitative susceptibility mapping using structural consistency between the magnitude image and the susceptibility map. *Neuroimage* 2012; 59: 2560–2568.
24. Bilgic B, Fan AP, Polimeni JR, Cauley SF, Bianciardi M, Adalsteinsson E, Wald LL, Setsompop K. Fast quantitative susceptibility mapping with L1-regularization and automatic parameter selection. *Magn. Reson. Med.* 2014; 72: 1444–1459.
25. Schweser F, Sommer K, Deistung A, Reichenbach JR. Quantitative susceptibility mapping for investigating subtle susceptibility variations in the human brain. *Neuroimage* 2012; 62: 2083–2100.
26. Bredies K, Kunisch K, Pock T. Total generalized variation. *Siam J. Imaging Sci.* 2010; 3: 492–526.
27. Bredies K, Ropele S, Poser BA, Barth M, Langkammer C. Single-step quantitative susceptibility mapping using total generalized variation and 3D EPI. *Proceedings of the 22nd Annual Meeting ISMRM, Milan, Italy, 2014*; 62: 604.
28. Langkammer C, Bredies K, Poser BA, Barth M, Reishofer G, Fan AP, Bilgic B, Fazekas F, Mainero C, Ropele S. Fast quantitative susceptibility mapping using 3D EPI and total generalized variation. *Neuroimage* 2015; 111: 622–630.
29. Liu T, Spincemaille P, de Rochefort L, Kressler B, Wang Y. Calculation of susceptibility through multiple orientation sampling (COSMOS): a method for conditioning the inverse problem from measured magnetic field map to susceptibility source image in MRI. *Magn. Reson. Med.* 2009; 61: 196–204.
30. Bilgic B, Xie L, Dobb R, Langkammer C, Mutluy A, Ye H, Polimeni JR, Augustinack J, Liu C, Wald LL, Setsompop K. Rapid multi-orientation quantitative susceptibility mapping. *Neuroimage* 2015; 125: 1131–1141.
31. Khabipova D, Wiaux Y, Gruetter R, Marques JP. A modulated closed form solution for quantitative susceptibility mapping—a thorough evaluation and comparison to iterative methods based on edge prior knowledge. *Neuroimage* 2015; 107: 163–174.
32. Wharton S, Bowtell R. Whole-brain susceptibility mapping at high field: a comparison of multiple- and single-orientation methods. *Neuroimage* 2010; 53: 515–525.
33. Sharma S, Hernando D, Horgn D, Reeder S. A joint background field removal and dipole deconvolution approach for quantitative susceptibility mapping in the liver. *Proceedings of the 22nd Annual Meeting ISMRM, Milan, Italy, 2014*; 606.
34. Liu T, Zhou D, Spincemaille P, Yi W. Differential approach to quantitative susceptibility mapping without background field removal. *Proceedings of the 22nd Annual Meeting ISMRM, Milan, Italy, 2014*; 597.
35. Bilgic B, Langkammer C, Wald LL, Setsompop K. Single-step QSM with fast reconstruction. *Third International Workshop on MRI Phase Contrast & Quantitative Susceptibility Mapping, Durham, NC, USA, 2014*.
36. Chambolle A, Pock T. A first-order primal-dual algorithm for convex problems with applications to imaging. *J. Math. Imaging Vis.* 2011; 40: 120–145.
37. Bilgic B, Gagoski BA, Cauley SF, Fan AP, Polimeni JR, Grant PE, Wald LL, Setsompop K. Wave-CAIPI for highly accelerated 3D imaging. *Magn. Reson. Med.* 2015; 73: 2152–2162.
38. Buehrer M, Boesiger P, Kozerke S. Virtual body coil calibration for phased-array imaging. *Proceedings of the 17th Annual Meeting ISMRM, Honolulu, HI, USA, 2009*; 760.
39. Uecker M, Lai P, Murphy M, Virtue P, Elad M, Pauly JM, Vasanawala S, Lustig M. ESPIRiT—an eigenvalue approach to autocalibrating parallel MRI: where SENSE meets GRAPPA. *Magn. Reson. Med.* 2014; 71: 990–1001.
40. Glowinski R, Marroco A. Sur l'approximation, par éléments finis d'ordre un, et la résolution, par pénalisation-dualité d'une classe de problèmes de Dirichlet non linéaires. *Rev. Fr. Automat. Inform. Rech. Op.* 1975; 9: 41–76.
41. Gabay D, Mercier B. A dual algorithm for the solution of nonlinear variational problems via finite element approximation. *Comput. Math. Appl.* 1976; 2: 17–40.
42. Fortin M, Glowinski R. Augmented Lagrangian methods: applications to the numerical solution of boundary-value problems. In *Augmented Lagrangian Methods: Applications to the Numerical Solution of Boundary-Value Problems*. Publisher: Town, 1983.
43. Bertsekas DP, Tsitsiklis JN. *Parallel and Distributed Computation: Numerical Methods*. Publisher: Town, 1989.
44. Eckstein J, Bertsekas DP. On the Douglas-Rachford splitting method and the proximal point algorithm for maximal monotone operators. *Math. Program.* 1992; 55: 293–318.
45. Fukushima M. Application of the alternating direction method of multipliers to separable convex programming problems. *Comput. Optim. Appl.* 1992; 1: 93–111.

46. Eckstein J, Fukushima M. Some reformulations and applications of the alternating direction method of multipliers. *Large Scale Optim. State Art* 1993; 119–138.
47. Chen G, Teboulle M. A proximal-based decomposition method for convex minimization problems. *Math. Program.* 1994; 64: 81–101.
48. Boyd S, Parikh N, Chu E, Peleato B, Eckstein J. Distributed optimization and statistical learning via the alternating direction method of multipliers. *Trends Mach. Learn.* 2010; 3: 1–122.
49. Wu B, Li W, Guidon A, Liu C. Whole brain susceptibility mapping using compressed sensing. *Magn. Reson. Med.* 2012; 67: 137–147.
50. Li W, Avram AV, Wu B, Xiao X, Liu C. Integrated Laplacian-based phase unwrapping and background phase removal for quantitative susceptibility mapping. *NMR Biomed.* 2014; 27: 219–227.
51. Knoll F, Bredies K, Pock T, Stollberger R. Second order total generalized variation (TGV) for MRI. *Magn. Reson. Med.* 2011; 65: 480–491.
52. Schofield MA, Zhu Y. Fast phase unwrapping algorithm for interferometric applications. *Opt. Lett.* 2003; 28: 1194.
53. Hansen PC. *The L-Curve and its Use in the Numerical Treatment of Inverse Problems*. WIT Press: Southampton, 2000.
54. Christ A, Kainz W, Hahn E. The Virtual Family—development of surface-based anatomical models of two adults and two children for dosimetric simulations. *Phys. Med. Biol.* 2010; 55: N23.
55. Wisnieff C, Liu T, Spincemaille P, Wang S, Zhou D, Wang Y. Magnetic susceptibility anisotropy: cylindrical symmetry from macroscopically ordered anisotropic molecules and accuracy of MRI measurements using few orientations. *Neuroimage* 2013; 70: 363–376.
56. Poser BA, Koopmans PJ, Witzel T, Wald LL, Barth M. Three dimensional echo-planar imaging at 7 Tesla. *Neuroimage* 2010; 51: 261–266.
57. Gagoski B, Bilgic B, Eichner C. RARE/turbo spin echo imaging with simultaneous multislice Wave-CAIPI. *Magn. Reson. Med.* 2015; 73: 929–938.
58. Pruessmann K, Weiger M, Scheidegger MB, Boesiger P. SENSE: sensitivity encoding for fast MRI. *Magn. Reson. Med.* 1999; 42(5): 952–962.
59. Ramani S, Fessler JA. Parallel MR image reconstruction using augmented Lagrangian methods. *IEEE Trans. Med. Imaging* 2011; 30: 694–706.
60. Haacke E, Xu Y, Cheng YCN, Reichenbach JR. Susceptibility weighted imaging (SWI). *Magn. Reson. Med.* 2004; 52: 612–618.
61. Robinson S, Grabner G, Witoszynski S, Trattng S. Combining phase images from multi-channel RF coils using 3D phase offset maps derived from a dual-echo scan. *Magn. Reson. Med.* 2011; 65: 1638–1648.
62. Sumpf T, Uecker M. Model-based nonlinear inverse reconstruction for T2 mapping using highly undersampled spin-echo MRI. *J. Magn. Reson. Imaging* 2011; 34: 420–428.
63. Weller DS, Ramani S, Fessler JA. Augmented Lagrangian with variable splitting for faster non-cartesian L1-SPIRiT MR image reconstruction. *IEEE Trans. Med. Imaging* 2014; 33: 351–361.
64. Guo W, Qin J, Yin W. A new detail-preserving regularization scheme. *Siam J. Imaging Sci.* 2014; 7: 1309–1334.

## Supporting information

Additional supporting information can be found in the online version of this article at the publisher's website.

## APPENDIX

### CLOSED-FORM ITERATIONS FOR TOTAL GENERALIZED VARIATION (TGV)-REGULARIZED SINGLE-STEP QUANTITATIVE SUSCEPTIBILITY MAPPING (QSM)

Using the discrete version of the second-order TGV regularizer, recovery of the underlying magnetic susceptibility distribution involves solving the following optimization problem:

$$\min_{\chi, v} \frac{1}{2} \sum_i \left\| M_i F^{-1} H_i D F \chi - M_i F^{-1} H_i F \Psi(\phi) \right\|_2^2 + \alpha_1 \|\mathcal{G}\chi - v\|_1 + \alpha_0 \|\varepsilon(v)\|_1, \quad (\text{A1})$$

where  $\mathcal{G}$  is the three-dimensional gradient operator,  $\varepsilon$  is a

symmetrized derivative as defined in ref. (26), and  $\alpha_0$  and  $\alpha_1$  are regularization parameters. By introducing the additional variables  $z_0$ ,  $z_1$  and  $z_2$  with the consensus constraints, Equation (A1) becomes:

$$\min_{\chi, v, z_0, z_1, z_2} \frac{1}{2} \sum_i \left\| M_i F^{-1} z_{2,i} - M_i F^{-1} H_i F \Psi(\phi) \right\|_2^2 + \alpha_1 \|z_1\|_1 + \alpha_0 \|z_0\|_1, \quad (\text{A2})$$

subject to  $\varepsilon(v) = z_0$ ,  $\mathcal{G}\chi - v = z_1$  and  $H_i D F \chi = z_{2,i}$

To efficiently solve Equation (A2), we adopt the alternating direction method of multipliers (ADMM) (40–48) to decompose the original problem into smaller subproblems that are easy to solve.

The subproblem for the  $(\chi, v)$  pair is:

$$\min_{\chi, v} \frac{\mu_0}{2} \|\varepsilon(v) - (z_0 - s_0)\|_2^2 + \frac{\mu_1}{2} \|\mathcal{G}\chi - v - (z_1 - s_1)\|_2^2 + \frac{\mu_2}{2} \sum_i \left\| H_i D F \chi - (z_{2,i} - s_{2,i}) \right\|_2^2 \quad (\text{A3})$$

where  $s_0$ ,  $s_1$  and  $s_2$  are the scaled dual variables, and  $\mu_0$ ,  $\mu_1$  and  $\mu_2$  are the augmented Lagrangian parameters. Taking the gradients with respect to both  $\chi$  and  $v$  of Equation (A3) and setting them to zero yields the system of linear equations with circulant blocks. Diagonalizing each block by the discrete Fourier transform and then reordering the resulting diagonal-block matrix, we obtain the following system:

$$\begin{bmatrix} A_1 & & & \\ & A_2 & & \\ & & \ddots & \\ & & & A_N \end{bmatrix} \begin{bmatrix} u_1 \\ u_2 \\ \vdots \\ u_N \end{bmatrix} = \begin{bmatrix} b_1 \\ b_2 \\ \vdots \\ b_N \end{bmatrix} \quad (\text{A4})$$

where the  $A_n$  values are  $4 \times 4$  Hermitian positive definite matrices that represent the system associating with voxel  $n$ ,  $u_n = (F\chi_x, F\chi_y, F\chi_z)^T$  at voxel  $n$  and  $N$  is the number of voxels. We can update each  $u_n$  independently because the systems associated with the voxels are decoupled. Moreover, as the  $A_n$  values have small dimensions of  $4 \times 4$ , we can easily update  $u_n$  using many techniques, such as the factor-solve method, Cramer's rule and even a direct inversion (63,64).

The  $z_0$  and  $z_1$  updates can be performed using the voxel-wise soft-thresholding operations:

$$z_0 = \max \left( \left| (\varepsilon(v) + s_0)_{(n)} \right| - \frac{\alpha_0}{\mu_0}, 0 \right) \circ \text{sign} \left( (\varepsilon(v) + s_0)_{(n)} \right) \quad (\text{A5})$$

$$z_1 = \max \left( \left| (\mathcal{G}\chi - v + s_1)_{(n)} \right| - \frac{\alpha_1}{\mu_1}, 0 \right) \circ \text{sign} \left( (\mathcal{G}\chi - v + s_1)_{(n)} \right) \quad (\text{A6})$$

where  $\circ$  denotes the Hadamard product, and the subscript in parentheses is the voxel label.

The subproblem for  $z_2$  is:

$$\min_{z_2} \frac{1}{2} \sum_i \left\| M_i F^{-1} z_{2,i} - M_i F^{-1} H_i F \Psi(\phi) \right\|_2^2 + \frac{\mu_2}{2} \sum_i \left\| z_{2,i} - (H_i D F \chi + s_{2,i}) \right\|_2^2 \quad (\text{A7})$$

The systems associated with the  $z_{2,i}$  values are decoupled, and so we can update each  $z_{2,i}$  independently. By taking the gradient of Equation (A7) with respect to  $z_{2,i}$  and setting it to zero, we obtain the following analytical solution:

$$z_{2,i} = F(M_i^* M_i + \mu_2 I)^{-1} (M_i^* M_i F^{-1} H_i F \Psi(\phi) + \mu_2 F^{-1} (H_i D F \chi + s_{2,i})) \quad (\text{A8})$$

$$s_1 := s_1 + G \chi - v - z_1 \quad (\text{A10})$$

$$s_{2,i} := s_{2,i} + H_i D F \chi - z_{2,i} \quad (\text{A11})$$

We can precompute  $M_i^* M_i F^{-1} H_i F \Psi(\phi)$  and  $(M_i^* M_i + \mu_2 I)^{-1}$ . It is trivial to compute the inverse of  $M_i^* M_i + \mu_2 I$  because it is a diagonal matrix. As a result, we only need two fast Fourier transform operations and a few matrix multiplications and matrix additions for each  $z_{2,i}$  update.

In summary, the TGV-regularized single-step QSM is solved by iterating Equations (A4–A6) and (A8–A11) until convergence, as implemented in the accompanying MATLAB code. The TV-regularized single-step QSM implementation can be derived using the same approach. [Please see the accompanying MATLAB code for the implementation.]

Finally, we can update the scaled dual variables as follows:

$$s_0 := s_0 + \varepsilon(v) - z_0 \quad (\text{A9})$$